

Hexagonal Boron Nitride Threshold Memristors with Nickel Electrodes

Lukas Völkel¹, Dennis Braun¹, Melkamu Belete¹, Satender Kataria¹, Thorsten Wahlbrink², Ke Ran^{3,4},

Kevin Kistermann³, Joachim Mayer^{3,4}, Stephan Menzel⁵, Alwin Daus^{1}, Max C. Lemme^{1,2*}*

¹Chair of Electronic Devices, RWTH Aachen University, Otto-Blumenthal-Str. 2, 52074 Aachen, Germany.

² AMO GmbH, Advanced Microelectronic Center Aachen, Otto-Blumenthal-Str. 25, 52074 Aachen, Germany.

³ Central Facility for Electron Microscopy (GFE), RWTH Aachen University, Ahornstr. 55, 52074, Aachen, Germany.

⁴ Ernst Ruska-Centre for Microscopy and Spectroscopy with Electrons (ER-C 2), Forschungszentrum Jülich, 52425, Jülich, Germany.

⁵ Peter Gruenberg Institute (PGI-7), Forschungszentrum Juelich GmbH and JARA-FIT, 52425 Juelich, Germany.

*Corresponding authors: max.lemme@eld.rwth-aachen.de, alwin.daus@eld.rwth-aachen.de

Keywords: memristor, threshold switching, hexagonal boron nitride, filament, 2D materials

Abstract:

Two-dimensional (2D) materials have attracted much attention as the active medium in memristors for next generation computing hardware solutions like in-memory computing or neuromorphic computing. Hexagonal boron nitride (h-BN) is particularly promising due to its insulating property which enables low stand-by currents and a large switching window. Volatile (threshold) resistive switching in h-BN devices is of specific interest for certain synaptic/neuronal functions in neuromorphic circuits and is useful for selectors in crossbar arrays. Here we present a complementary metal-oxide semiconductor technology (CMOS) compatible, multilayer h-BN based threshold memristor with a wide and tunable current operation range and low stand-by currents. The switching characteristics of our devices are comparable to other h-BN based threshold switches in literature. In addition, our results show a low cycle-to-cycle variability of 5 %. We also provide a detailed study of the current conduction mechanism of our devices in the high and low resistance states by performing temperature-dependent current-voltage measurements. Supported by transmission electron microscopy analysis, we propose the formation and retraction of nickel-filaments along boron defects in the h-BN film as the resistive switching mechanism. Thus, we demonstrate that temperature-dependent current-voltage analysis is a valuable tool for analyzing resistive switching phenomena in 2D-material based memristors.

1. Introduction

The need for processing constantly growing data volumes poses challenges to classical computing hardware based on the von Neumann architecture, which can potentially be overcome by new approaches like in-memory computing or neuromorphic computing (NC)^[1-3]. Energy efficiency is a particular and major concern, which calls for new types of devices to be combined with complementary metal-oxide semiconductor (CMOS) technology, e.g. resistive switching (RS) devices. Among those, threshold resistive switching (TS) devices provide specific properties useful for NC, such as performing certain synaptic and neural functions^[4,5] or serving as selectors in crossbar arrays^[6,7]. TS is characterized by a sudden decrease in device resistance upon applying a voltage above a certain threshold level, followed by a hysteretic self-recovery when the voltage is removed^[8]. Two-dimensional (2D) materials have caught the attention of the semiconductor materials and devices community because of their promising switching performance, high-integration density capability, ultimate scalability, potential for low power consumption, and compatibility with conventional CMOS technology^[9-11]. Different underlying RS mechanisms like ionic transport^[12], conductive-filament formation^[13], or phase change effects^[14] have been proposed for 2D materials.

Hexagonal boron nitride (h-BN) is a particularly interesting candidate for 2D-material-based RS devices due to its high thermal conductivity, thermal and chemical stability, dangling bond-free surface, and

wide bandgap (~ 5.9 eV) that enables a large switching window ^[15–18]. Previously, 2D h-BN has been reported to exhibit TS^[19–21] and non-volatile RS^[17,22–25]. To the best of our knowledge, most h-BN-based devices reported in literature either lack a CMOS-compatible configuration^[7,17,20,26–33], or provide only single current-voltage (*I*-*V*) curves ^[22,27,34]. In addition, there is little information from detailed electrical analyses of the underlying current conduction mechanisms, despite being a valuable method to extract information about defects and their role in the carrier transport, which provides insights into the RS mechanism^[35]. Mostly, metal filament formation is suggested for h-BN devices as the RS mechanism ^[19,25,27,32,36], usually supported by methods other than the analysis of the current conduction mechanism. A few publications discuss the current conduction mechanism of monolayer h-BN-based devices^[22,28] while the current conduction mechanism for multilayer h-BN in a memristor structure is still unknown.

Here, we present CMOS-compatible nickel (Ni)/h-BN/Ni cross-point TS devices with low cycle-to-cycle variability. We investigate the current conduction mechanism for both high and low resistance states through temperature-dependent *I*-*V* measurements. Based on the extracted current conduction mechanism and transmission electron microscopy (TEM) images, we propose metal-filament formation across the h-BN films and subsequent self-rupture as the TS mechanism in our h-BN memristors.

2. Results and discussion

Figure 1a shows a schematic of our fabricated cross-point devices with h-BN sandwiched between two Ni electrodes. The bottom electrode (BE) and the top electrode (TE) were patterned with optical lithography followed by 60 nm Ni sputtering and lift-off. H-BN was transferred using a polymer-assisted wet-chemical transfer method (see Experimental Methods). Two h-BN films were stacked on top of each other through subsequent transfer processes to minimize the formation of cracks and macroscopic defects. Possible photoresist residues or wrinkles from the transfer are not expected to influence the RS behavior in our devices as they only increase the film resistance locally and therefore suppress filament formation only at those locations, as shown for h-BN based memristive circuits^[37]. In particular, the fact that the resist was not exposed to plasma processing prior to its removal minimizes residues. An additional 50 nm thick aluminum (Al) layer was sputtered on top of both Ni contact pads after TE deposition to provide a good electrical contact between the device and the probe needles during measurements. The active area of the devices was measured to be $34 \mu\text{m}^2$. A possible impact of nickel-oxide formation between the Ni and the Al at the contact pads on the RS behavior is excluded by *I*-*V* measurements on Ni/Ni control devices without h-BN between the electrodes (supporting information Figure S2). Figure 1b shows a top-view optical microscope image of a fabricated cross-point device. Reactive ion etching (RIE) was carried out to remove the h-BN films from

the Al contact pad area and led to polymer residues. However, this is not expected to influence the device performance as the etching was done after the intrinsic device stack of Ni/h-BN/Ni was fully assembled. More details about the fabrication methods are available in the Experimental Methods section, and a schematic process flow is shown in Figure S1 in the supporting information. Figure 1c presents a top-view optical microscope image of the boundary area showing both the first transferred h-BN film and the stack of the two films. The inset Raman map shows the integrated peak intensity around the characteristic E_{2g} peak of bulk h-BN at 1366 cm^{-1} .^[38] The region with only one h-BN film is clearly distinguishable from that with two h-BN films due to the overall higher peak intensity for the thicker film. However, the visibly patchy structure indicates a spatial variation of h-BN layer numbers in both regions^[16,38]. A histogram of all peak positions from the Raman map and a Gaussian distribution fit are shown in Figure S3 in the supporting information. The mean peak position is at $1367.0 \pm 0.9\text{ cm}^{-1}$, indicating 3-layer to bulk h-BN^[16]. Figure 1d shows four spectra extracted from the positions marked in the Raman map in Figure 1c. The peak position only marginally changes for the different measurement positions, whereas the peak height is increased at the brighter positions compared to the darker ones, confirming a non-uniform h-BN thickness. A scanning electron microscopy (SEM) image of the two stacked h-BN films shows white triangles, identified as multilayer nucleation sites, in front of a darker background, supporting the findings from the Raman measurements (Figure 1e). A high-resolution TEM (HRTEM) cross-section image of a fabricated device is presented in Figure 1f. The layered 2D nature of the multilayer h-BN film is clearly visible with an interlayer distance of $3.3 \pm 0.02\text{ \AA}$, which is in good agreement with values reported in literature^[39,40]. The boundary between the two transferred h-BN films manifests in a deviation of the layer distance between two adjacent layers of almost 30 % (see supporting information section S4). The first and second transferred h-BN films are highlighted in blue and orange, respectively. It was estimated from the HRTEM image that the h-BN devices (consisting of the two transferred films) have an average thickness of $5 \pm 0.5\text{ nm}$.

I-V characterization was performed on cross-point devices. Figure 2a shows five subsequent voltage sweeps from 0 V to 3 V and back to 0 V with a sweep rate of $\sim 0.33\text{ V/s}$, which were applied to the top electrode of a device while the bottom electrode was grounded (see inset of Figure 2a). The device is initially in a high resistance state (HRS) but changes abruptly to a low resistance state (LRS) during the forward sweep (indicated with arrow number 1) at an on-threshold voltage ($V_{th, on}$) of $\sim 2.1\text{ V}$. The current compliance (CC) was set to 10 nA for this measurement. The device initially remains in LRS when the voltage is swept back towards 0 V, but eventually switches back to the HRS (arrow number 2), leading to an *I-V* hysteresis. The voltage at which the current level of the backward sweep reaches the initial level of the HRS is defined as the off-threshold voltage $V_{th, off}$. The device exhibited reproducible TS behavior^[4] with a current level below the noise limit of the measurement setup (1 pA) for voltages below 0.3 V in the HRS. Such low currents in the HRS open up the possibility to use our

devices as selectors for nonvolatile resistive switching cells^[7]. As an indirect measure for endurance, we plot the extracted $V_{th,on}$ and $V_{th,off}$ of ~ 600 subsequent cycles in a histogram (Figure 2b). We observe a tight distribution of $V_{th,on}$ and $V_{th,off}$ by fitting a Gaussian distribution curve to the data with the centers at 2 V and 0.3 V, respectively. The distribution width σ of 0.1 V for $V_{th,on}$ and $V_{th,off}$ indicates a low cycle-to-cycle variability of $V_{th,on}$ of 5 %, which is in same range of the best prior reported cycle-to-cycle variability of bipolar resistive switching in few-layer h-BN devices^[24]. The complete set of I - V curves of the endurance measurement is plotted in the supporting information (Figure S5). The inset of Figure 2b shows the normalized cumulative distribution functions (CDF) of the $V_{th,on}$ and $V_{th,off}$ distributions. Our devices exhibit TS behavior over three orders of magnitude of CC (Figure 2c). Typical TS behavior is visible for each CC. We extract an average $V_{th,on}$ of 2.0 ± 0.1 V, consistent with the value extracted from the endurance measurement, which implies that the CC does not influence the cycle-to-cycle variability considerably. Our devices compare well with h-BN based TS devices previously reported in literature although we used entirely CMOS compatible materials (see supporting information Table S6).

Next, we performed I - V sweep cycling on five different devices and set different CCs for each device to investigate the device-to-device variability (as discussed for Figure 2c, the CC does not influence the $V_{th,on}$ variability). Boxplots of the extracted $V_{th,on}$ for each device and the respective CC are shown in Figure 2d. The corresponding single data points are plotted in the background of each boxplot. Devices D2, D4, and D5 show a rather similar $V_{th,on}$ of ~ 1.9 V, whereas devices D1 and D3 deviate considerably with $V_{th,on} \approx 2.45$ V. We attribute this device-to-device variability to the inhomogeneous h-BN film thickness, and we would expect a smaller variability for more homogeneous h-BN films.

An important contribution towards understanding the RS mechanism can be expected from investigating the current conduction mechanism in both HRS and LRS regimes. There are different current conduction mechanisms discussed in literature for electron transport across dielectrics, including Fowler-Nordheim tunneling, Schottky emission, Poole-Frenkel emission, and many others^[35,41]. Current conduction mechanisms can be roughly classified into injection-limited, where the carrier transport depends on the metal-dielectric contact, and bulk-limited mechanisms, where the electrical transport depends on the properties of the dielectric itself^[41]. Thermally activated current conduction mechanisms can be analyzed by temperature-dependent I - V measurements, which allows extracting physical parameters like the charge carrier mobility, trap energies, or the dielectric constant. The dominating current conduction mechanism can be determined with reasonable certainty by evaluating the goodness of the model's fit to the experimental data, although the validity of the extracted physical parameters should always be considered.

First, we analyzed the current conduction mechanism in HRS by performing temperature-dependent *I*-*V* measurements on a device in its HRS with a maximum applied voltage well below $V_{th, on}$. The device resistance and *I*-*V* sweeps were subsequently measured at different temperatures (for more details see Experimental Methods). Smoothened *I*-*V* curves for different temperatures between 60 K and 260 K are plotted in Figure 3a (the unprocessed data is provided in the supporting information section S7). The current level of the non-linear *I*-*V* characteristic increases with temperature (Figure 3b). Direct tunneling, Fowler-Nordheim tunneling, Schottky emission, and thermionic field emission are injection-limited current conduction mechanisms^[41]. Fowler-Nordheim tunneling and direct tunneling have a weak temperature dependence, so that we can easily exclude them given the clear temperature dependence observed in Figure 3a. Given the fact that h-BN has a bandgap of \sim 6 eV^[42] and that we measure at low temperatures \leq 260 K, Schottky- and thermionic field-emission are also very unlikely in our device. From the class of bulk-limited current conduction mechanisms, we will discuss Poole-Frenkel conduction^[43–45], space-charge limited conduction (SCLC)^[43,46,47], nearest neighbor hopping^[48] (NNH), Mott variable range hopping^[48] (VRH), hopping conduction^[48,49], and trap assisted tunneling (TAT)^[50,51]. We took the coefficient of determination, denoted R^2 , to compare the goodness of the fits for the different current conduction mechanisms (see section S9 in the supporting information for more information). An Arrhenius plot of the *I*-*V* curves from Figure 3a displays the natural logarithm of the current density versus the inverse temperature for four different voltages (Figure 3c). Two linear regimes can be identified in the Arrhenius curves, one in the temperature range from 60 K to 120 K, and the other in the temperature range from 160 K to 260 K. To visualize this, we fitted the measured data to a linear regression line in these two temperature regimes, which initially suggests the existence of two different current conduction mechanisms, each dominating in one of the respective temperature regimes. The R^2 -values for the fits in the higher temperature range are between 0.8 and 0.9, indicating a reasonable level of correlation between the data and the model used. However, the R^2 -values for the fits in the lower temperature range lie between 0.4 and 0.8, i.e. a weak correlation. In addition, the slope of the fit for 0.26 V is positive, opposite to the higher voltages. We attribute this inconclusive result to the combination of a low temperature with a low voltage, which led to an unreliable trend due to very low current levels of < 2 pA, which is close to the noise level of our measurement equipment (see Figure S7). Thus, we cannot conclusively confirm two different current conduction mechanism regimes for different temperatures.

To find the current conduction mechanism that matches best to our *I*-*V* curves, we linearized our data according to the current conduction mechanism theory and performed a linear regression on such data. We developed an automated algorithm to obtain the most linear region in the linearized data according to the R^2 -criterion. A detailed explanation of the algorithm can be found in the supporting information section S8. We excluded the voltage range and corresponding values of the linearized data

between 0 V and 0.26 V because of the high noise present in this range (Figure 3c). Applying the R^2 -method to the Poole-Frenkel conduction, SCLC, and NNH current conduction mechanisms we can find parts in our I - V data with good linearity. However, using the extracted fit parameters to calculate the corresponding physical quantities leads to unreasonable values, so we excluded those as possible current conduction mechanisms in the HRS of our devices. To be precise, we extracted a dielectric constant of h-BN between 319 and 6281 for the Poole-Frenkel conduction, an unreasonably high concentration of free charge carriers of around 10^{17} cm⁻³ for SCLC, and a negative hopping energy for NNH (see section S9 in the supporting information for more details). Analyzing the Mott VRH model leads to reasonable physical parameters, but the model can only describe our data for temperatures ≥ 160 K at an applied voltage of 0.1 V, which severely limits its applicability in our case. The detailed discussion can be found in the supporting information in section S9. In the following, we discuss the hopping conduction and TAT theory in more detail, which we believe match best to our device characteristics.

In the hopping conduction theory, electrons tunnel through the insulator with the help of traps which effectively narrow the barrier width. Although the carrier energy is lower than the maximum energy of the potential barrier the carriers can still transit using the tunnel mechanism^[41]. The current density depends on the temperature and the electric field as follows:^[52]

$$J = qnva \exp\left(\frac{qaE}{k_B T} - \frac{\Phi_t}{k_B T}\right), \quad (1)$$

where q is the elementary charge, n the electron concentration in the conduction band, v the frequency of thermal vibrations of electrons at trap sites, E the applied electric field, k_B the Boltzmann constant, T the temperature, a the mean distance between the trap sites (i.e., hopping distance), and Φ_t the energy level difference between the trap states and the conduction band minimum (see Figure 3d, left). The hopping distance can be extracted from the slope of the linear part in the characteristic hopping conduction plot ($\ln(J)$ vs. E), shown in Figure 3e. The I - V data for each temperature is plotted with a small offset for better visibility (original data: supporting information Figure S10). The region with the gray background is the most linear region according to our R^2 -algorithm (0.26 V – 0.8 V, $R^2 = 0.992$). The colored lines are the corresponding linear fits. The hopping distance was determined to be 2.5 ± 1.3 Å, which seems to be a reasonable (minimum) value taking note that the minimum trap distance in the current flow direction should be given by the h-BN layer spacing (~ 3.3 Å, see Figure 1f and supporting information section S4). The trap energy level is extracted from the slope of the linear region in the Arrhenius plot for every applied electric field between 0.56 MV/cm (0.28 V) and 1.6 MV/cm (0.8 V), and we obtain a value of $\Phi_t = 51 \pm 16$ meV. The errors of the hopping distance and the trap energy are relatively large, which resembles, in a band diagram picture, the Mott VRH current conduction mechanism, where the charge carriers tunnel via traps with varying distance and energy

level^[35]. The analysis of the Mott VRH current conduction mechanism is based on the measurement shown in Fig. 3b and exhibit a hopping energy barrier E_h (corresponding to Φ_t in the hopping conduction model) of 36 ± 6 meV at a voltage of 0.1 V (see supporting information section S10). This fits well to the extracted Φ_t in the hopping conduction theory and supports our hypothesis that the current conduction in the HRS in our devices in the low voltage regime is defect mediated.

In TAT, it is assumed that electrons tunnel through the insulator with the help of only one trap site at a certain energy Φ_t below the conduction band minimum^[50] (see Figure 3d, right). Its current density is given as^[35]

$$J = A \cdot \exp\left(\frac{-4\sqrt{2qm_{eff}}}{3\hbar E} \phi_t^{3/2}\right), \quad (2)$$

where A is a proportionality constant, m_{eff} the electron effective mass, and \hbar the reduced Planck constant. Φ_t can be extracted from the slope of the linear part in the characteristic TAT plot, shown in Figure 3f. The most linear part according to our R^2 -algorithm is between 0.68 V and 1 V ($R^2 = 0.99998$) and is indicated with a gray background in Figure 3f. The lines represent again the corresponding linear fits of the data and are plotted once more with a small offset for better visibility (original data in Figure S11). We extract a mean trap energy of $\Phi_t = 0.11 \pm 0.01$ eV by assuming $m_{eff} = 2.21m_e$ ^[53], where m_e is the electron mass. This energy level is in good accordance with the extracted trap energy levels at smaller voltages in the hopping conduction and Mott VRH regime. In conclusion, hopping conduction and TAT current conduction mechanisms match best our temperature-dependent I - V data in a voltage range between 0.26 V and 1 V, while the Mott VRH current conduction mechanism can be used to describe our experimental data at 0.1 V for temperatures ≥ 160 K. All plausible current conduction mechanisms are based on defect-supported electron hopping through the h-BN. We therefore summarize that defects play a crucial role in the current conduction in the HRS.

We also performed temperature-dependent measurements on a device in a permanent LRS, which was formed by repeated I - V switching cycles at high CC (500 nA). This was necessary because under normal operation, the devices always fall back to the HRS once the bias voltage is tuned back towards 0 V. Temperature-dependent I - V curves in a temperature range between 60 K and 260 K are shown in Figure 4a. The current linearly depends on the voltage and the current level decreases with increasing temperature. All curves exhibit a slope very close to 1 when plotted in a double-logarithmic scale (see supporting information Figure S12), indicating ohmic conduction as the dominating current conduction mechanism^[43]. The resistance vs. temperature is plotted in Figure 4b. The resistance linearly decreases at higher temperatures and saturates at ~ 360 Ω for temperatures below 80 K. The observed relation between the resistance and temperature can be explained by Matthiessen's rule, which states that the dependence of the resistivity of metals on the temperature is^[54]

$$\rho(T) = \rho_0 + \rho_{ph}(T), \quad (3)$$

where ρ_0 is the residual resistivity, which comprises all structural resistivity contributions like defect or surface scattering, and $\rho_{ph}(T)$ is the resistivity contribution due to electron-phonon scattering. For metals, $\rho_{ph}(T)$ depends linearly on temperature at high temperatures and the temperature dependent resistance can be described as^[55]

$$R(T) = R_0[1 + \alpha(T - T_0)], \quad (4)$$

where R_0 is a certain resistance at temperature T_0 (often $T_0 = 0$ K), and α is a material-specific temperature coefficient. By fitting the temperature region $T \geq 160$ K we extracted a temperature coefficient α of 0.0056 K⁻¹, which is close to the literature value of the temperature coefficient of nickel (0.006 K⁻¹)^[56]. Thus, we deduce that a stable Ni filament has been formed during repeated cycling with high CC.

For metallic filament formation, Ni ions must move through the h-BN layer under an applied voltage. Thus, the sweep rate, which is a measure of how long the voltage is applied at each measurement point, should influence $V_{th, on}$. We performed such sweep rate-dependent measurements on a TS device and plotted the results in Figure 4c. Although there is a visible fluctuation of $V_{th, on}$ we observe a clear trend that $V_{th, on}$ increases with increasing sweep rate, in line with our expectations. At smaller sweep rates the Ni ions have more time per voltage to move through the h-BN and reach the opposite electrode already at smaller $V_{th, on}$ values compared to higher sweep rates. Figure 4d (top) displays a TEM image of a device cross-section in a permanent LRS, reached after several *I*-*V* cycles, with the bright part representing the h-BN layer. In Figure 4d (bottom), we overlay the TEM cross-sectional image with energy filtered TEM (EFTEM) images of Ni (purple) and boron (B, green). The B layer exhibits three defective regions of several nm width, highlighted by three white arrows. At these positions, the Ni electrodes are in direct contact with each other, whereas they are well separated by the h-BN layer in the rest of the image. In h-BN, the generation of B vacancies is favored compared to the formation of nitrogen (N) vacancies, which results in a higher density of N-terminated B vacancies^[57]. In the EFTEM image of nitrogen (supporting information Figure S13) no distinct defects are visible in the h-BN film. This leads to the assumption that B vacancies are responsible for mediating the Ni-filament formation. The importance of B vacancies for RS of h-BN between inert electrodes was recently shown in an ab initio study of RS in two- and three-layer hexagonal boron nitride between two graphene electrodes^[58], which supports our findings. Based on our observations and corresponding literature, we propose Ni ion diffusion through the h-BN film at B vacancies and subsequent Ni-filament formation when a positive voltage is applied to the top electrode. The facts that we observe TS behavior over three orders of magnitude of current (see Fig. 2c) and that we measure currents in the mA range after setting a device to a permanent LRS (see Fig. 4a) indicate that the filament growth is not complete

when the CC limits the current. Thus, there is no direct metal contact between both electrodes and the filaments dissolve when the voltage is removed, enabling TS. The increase of the current over orders of magnitude can be explained by a decrease of the tunnel distance between the growing filaments and the counter electrode^[59]. When the current through the device increases, e.g. by increasing the compliance, the filament-electrode gap decreases, and the filament needs longer time to dissolve^[60]. Thus, repeated cycling at high CC can lead to a permanent LRS state with both electrodes in contact via a stable metal filament. From our TEM findings (see Fig. 4d) we deduce that not only one, but multiple filaments are formed during cycling.

3. Conclusion

We demonstrated threshold switching memristors in a cross-point structure based on mechanically stacked h-BN films implemented with a fully CMOS-compatible process and material stack. The DC-endurance of the devices was shown in \sim 600 voltage sweeps and exhibited a low $V_{th, on}$ cycle-to-cycle variability of 5 %. Furthermore, we conducted a detailed study of the current conduction mechanisms in high and low resistive state, which has not been reported for multilayer h-BN memristors. Three different current conduction mechanisms can be discerned in the HRS: Mott variable range hopping, hopping conduction, and trap assisted tunneling. All imply that defects play a distinct role in RS in h-BN. Characteristic ohmic conduction via Ni was found to be the dominating current conduction mechanism in the LRS. We propose Ni ion diffusion and filament formation at boron defect sites as the RS mechanism. This is consistent with the direct observation of multiple Ni filaments with TEM investigations and sweep rate-dependent I - V measurements.

4. Experimental Methods

Device Fabrication: 2 cm x 2 cm Si chips covered with 90 nm thermal SiO₂ were used as substrates. The bottom electrodes (BE) were defined with a double layer resist stack (LOR 3A/AZ5214E from MicroChemicals GmbH/Merck Performance Materials GmbH) and optical contact lithography with an EVG 420 Mask Aligner. 60 nm of nickel (Ni) were deposited via direct current (DC) sputtering in a vonArdenne sputter tool “CS 730 S” and subsequent lift-off in a 150 C Dimethyl sulfoxide (DMSO) solution. Commercial few-layer hexagonal boron nitride (h-BN) grown on copper (Cu) foil by chemical vapor deposition (CVD) was wet-transferred with the support of a Polymethyl methacrylate (PMMA) layer. The PMMA was spin-coated onto the h-BN/Cu foil and the growth substrate was etched in an HCl + H₂O₂ + H₂O solution. To clean the h-BN from the etchant we let the PMMA/h-BN film float on DI-water over night. After cleaning, the polymer/h-BN stack was transferred onto the SiO₂/Si substrate. The h-BN multilayer films thus consist of two stacked few-layer h-BN films^[21]. The top electrode (TE) was defined by spin-coating of AZ5214E resist and optical contact lithography (EVG 420 Mask Aligner), sputtering of 60 nm Ni in DC-mode and subsequent lift-off in hot acetone. Contact lithography and 90 s

of reactive ion etching (RIE) in an Oxford-instruments-tool “Plasmalab System 100” with a mixture of nitrogen and oxygen gas were used to remove the h-BN from the bottom contact pads. A contact lithography step, 50 nm aluminum (Al) DC-sputtering and subsequent lift-off were performed to deposit Al contact pads. See supporting information Figure S1 for a schematic of the process flow.

Structural Device Analysis: Optical microscope images were recorded with a Leica INM100 microscope. Raman measurements were done with a WiTec Raman spectrometer alpha300R in mapping mode with an excitation laser wavelength of 532 nm with 10 mW laser power. Scanning electron microscope (SEM) images were recorded with a Zeiss Supra 60VP SEM at an operation voltage of 4 kV. The transmission electron microscope (TEM) investigations were done in two steps: First, a thin lamella was cut out of the middle of a cross point device with a FEI Strata400 system with a gallium (Ga) ion beam and placed on a Cu grid. Second, high resolution TEM (HRTEM) and energy-filtered TEM (EFTEM) images were recorded with a Fei Tecnai G² F20 S-TWIN system at 200 kV operation voltage.

Electrical Device Measurements: Electrical measurements were performed in a cryogenic probe station “CRX-6.5K” from LakeShore Cryotronics connected to a semiconductor parameter analyzer (SPA) “4200A-SCS” with two source measure unit (SMU) cards “Keithley 4200-SMU”, each connected to a pre-amplifier “Keithley 4200-PA” from Tektronix. The voltage was applied to the top electrode and the bottom electrode was grounded. Current-voltage (I - V) measurements were performed by sweeping the voltage from 0 V to a positive maximum voltage V_{max} and back to 0 V. Cycling measurements were done with a 20 s delay between each sweep cycle to give the possibly formed conductive filament more time to relax^[32]. The current is limited by an off-chip current limiter within the semiconductor parameter analyzer. Temperature-dependent measurements were performed in two steps, whereas the steps are repeated for each temperature: First, 15 measurement points at a constant read voltage of 100 mV were collected to extract the device resistance. In total, we measured the current for around one minute. Second, a forward sweep from -1 V to +1 V was applied. Sweep rate-dependent measurements were performed by varying the time the voltage is applied to the device before the current is measured. The set voltage ($V_{th,on}$) was automatically extracted by first smoothing the data with a Savitzky-Golay filter^[61], interpolating the data to get more data points at the position of rapid current increase, and searching for the maximum in the first derivative of the smoothed, interpolated data. The reset voltage ($V_{th,off}$) is defined as the voltage where the current falls below the noise limit of the SPA, i.e., the LRS and HRS state cannot be distinguished for voltages $< V_{th,off}$. The current density J was calculated by dividing the measured current by the active device area, which was measured with the optical microscope to be 34 μm^2 . The applied electric field was calculated by dividing the applied voltage by the h-BN thickness measured with the HRTEM image (Figure 1f).

Supporting Information

Supporting Information is available from the Wiley Online Library or from the author.

Acknowledgements

Financial support from the German Ministry of Education and Research, BMBF, within the projects NEUROTEC (16ES1134, 16ES1133K), NEUROTEC 2 (16ME0399, 16ME0398K, 16ME0400), and NeuroSys (03ZU1106AA, 03ZU1106BB) is gratefully acknowledged.

Conflict of Interest

The authors declare no conflict of interest.

Data Availability Statement

The data that support the findings of this study are available from the corresponding author upon reasonable request.

References:

- [1] E. García-Martín, C. F. Rodrigues, G. Riley, H. Grahn, *J. Parallel Distrib. Comput.* **2019**, *134*, 75.
- [2] E. Strubell, A. Ganesh, A. McCallum, In *Proceedings of the 57th Annual Meeting of the Association for Computational Linguistics*, Association for Computational Linguistics, Florence, Italy, **2019**, pp. 3645–3650.
- [3] M. Lanza, A. Sebastian, W. D. Lu, M. Le Gallo, M.-F. Chang, D. Akinwande, F. M. Puglisi, H. N. Alshareef, M. Liu, J. B. Roldan, *Science* **2022**, *376*, eabj9979.
- [4] M. Lanza, H.-S. P. Wong, E. Pop, D. Ielmini, D. Strukov, B. C. Regan, L. Larcher, M. A. Villena, J. J. Yang, L. Goux, A. Belmonte, Y. Yang, F. M. Puglisi, J. Kang, B. Magyari-Köpe, E. Yalon, A. Kenyon, M. Buckwell, A. Mehonic, A. Shluger, H. Li, T.-H. Hou, B. Hudec, D. Akinwande, R. Ge, S. Ambrogio, J. B. Roldan, E. Miranda, J. Suñe, K. L. Pey, X. Wu, N. Raghavan, E. Wu, W. D. Lu, G. Navarro, W. Zhang, H. Wu, R. Li, A. Holleitner, U. Wurstbauer, M. C. Lemme, M. Liu, S. Long, Q. Liu, H. Lv, A. Padovani, P. Pavan, I. Valov, X. Jing, T. Han, K. Zhu, S. Chen, F. Hui, Y. Shi, *Adv. Electron. Mater.* **2019**, *5*, 1800143.
- [5] A. Krishnaprasad, N. Choudhary, S. Das, D. Dev, H. Kalita, H.-S. Chung, O. Aina, Y. Jung, T. Roy, *Appl. Phys. Lett.* **2019**, *115*, 103104.
- [6] Q. Hua, H. Wu, B. Gao, M. Zhao, Y. Li, X. Li, X. Hou, M.-F. (Marvin) Chang, P. Zhou, H. Qian, *Adv. Sci.* **2019**, *6*, 1900024.
- [7] B. Yuan, X. Liang, L. Zhong, Y. Shi, F. Palumbo, S. Chen, F. Hui, X. Jing, M. A. Villena, L. Jiang, M. Lanza, *Adv. Electron. Mater.* **2020**, *6*, 1900115.
- [8] D. Ielmini, R. Waser, H. Akinaga, *Resistive switching: from fundamentals of nanoionic redox processes to memristive device applications*, **2016**.
- [9] G. Cao, P. Meng, J. Chen, H. Liu, R. Bian, C. Zhu, F. Liu, Z. Liu, *Adv. Funct. Mater.* **2021**, *31*, 2005443.
- [10] L. Yin, R. Cheng, Y. Wen, C. Liu, J. He, *Adv. Mater.* **2021**, *33*, 2007081.
- [11] M. C. Lemme, D. Akinwande, C. Huyghebaert, C. Stampfer, *Nat. Commun.* **2022**, *13*, 1392.
- [12] M. Belete, S. Kataria, A. Turfanda, S. Vaziri, T. Wahlbrink, O. Engström, M. C. Lemme, *Adv. Electron. Mater.* **2020**, *6*, 1900892.
- [13] S. M. Hus, R. Ge, P.-A. Chen, L. Liang, G. E. Donnelly, W. Ko, F. Huang, M.-H. Chiang, A.-P. Li, D. Akinwande, *Nat. Nanotechnol.* **2020**, *1*.
- [14] X. Zhu, D. Li, X. Liang, W. D. Lu, *Nat. Mater.* **2018**, *18*, 141.
- [15] K. K. Kim, A. Hsu, X. Jia, S. M. Kim, Y. Shi, M. Hofmann, D. Nezich, J. F. Rodriguez-Nieva, M. Dresselhaus, T. Palacios, J. Kong, *Nano Lett.* **2012**, *12*, 161.
- [16] L. H. Li, J. Cervenka, K. Watanabe, T. Taniguchi, Y. Chen, *ACS Nano* **2014**, *8*, 1457.
- [17] M. A. Villena, F. Hui, X. Liang, Y. Shi, B. Yuan, X. Jing, K. Zhu, S. Chen, M. Lanza, *Microelectron. Reliab.* **2019**, *102*, 113410.
- [18] W. Auwärter, *Surf. Sci. Rep.* **2019**, *74*, 1.
- [19] C. Pan, Y. Ji, N. Xiao, F. Hui, K. Tang, Y. Guo, X. Xie, F. M. Puglisi, L. Larcher, E. Miranda, L. Jiang, Y. Shi, I. Valov, P. C. McIntyre, R. Waser, M. Lanza, *Adv. Funct. Mater.* **2017**, *27*, 1604811.
- [20] F. Hui, M. A. Villena, W. Fang, A.-Y. Lu, J. Kong, Y. Shi, X. Jing, K. Zhu, M. Lanza, *2D Mater.* **2018**, *5*, 031011.
- [21] L. Völkel, D. Braun, M. Belete, S. Kataria, T. Wahlbrink, M. C. Lemme, In *2021 Silicon Nanoelectronics Workshop (SNW)*, **2021**, pp. 1–2.
- [22] X. Wu, R. Ge, P.-A. Chen, H. Chou, Z. Zhang, Y. Zhang, S. Banerjee, M.-H. Chiang, J. C. Lee, D. Akinwande, *Adv. Mater.* **2019**, *31*, 1806790.
- [23] P. Zhuang, W. Lin, J. Ahn, M. Catalano, H. Chou, A. Roy, M. Quevedo-Lopez, L. Colombo, W. Cai, S. K. Banerjee, *Adv. Electron. Mater.* **2020**, *6*, 1900979.
- [24] S. Chen, M. R. Mahmoodi, Y. Shi, C. Mahata, B. Yuan, X. Liang, C. Wen, F. Hui, D. Akinwande, D. B. Strukov, M. Lanza, *Nat. Electron.* **2020**, *3*, 638.
- [25] W. Lin, P. Zhuang, D. Akinwande, X.-A. Zhang, W. Cai, *Appl. Phys. Lett.* **2019**, *115*, 073101.
- [26] K. Qian, R. Y. Tay, V. C. Nguyen, J. Wang, G. Cai, T. Chen, E. H. T. Teo, P. S. Lee, *Adv. Funct. Mater.* **2016**, *26*, 2176.
- [27] Y. Li, Z. Cui, Y. He, H. Tian, T. Yang, C. Shou, J. Liu, *Appl. Phys. Lett.* **2022**, *120*, 173104.

[28] J. Ge, H. Huang, Z. Ma, W. Chen, X. Cao, H. Fang, J. Yan, Z. Liu, W. Wang, S. Pan, *Mater. Des.* **2021**, *198*, 109366.

[29] B. Wang, N. Xiao, C. Pan, Y. Shi, F. Hui, X. Jing, K. Zhu, B. Guo, M. A. Villena, E. Miranda, M. Lanza, *Cryst. Res. Technol.* **2018**, *53*, 1800006.

[30] G. Dastgeer, H. Abbas, D. Y. Kim, J. Eom, C. Choi, *Phys. Status Solidi RRL – Rapid Res. Lett.* **2020**, *15*, 2000473.

[31] R. D. Nikam, K. G. Rajput, H. Hwang, *Small* **2021**, *17*, 2006760.

[32] Y. Shi, X. Liang, B. Yuan, V. Chen, H. Li, F. Hui, Z. Yu, F. Yuan, E. Pop, H.-S. P. Wong, M. Lanza, *Nat. Electron.* **2018**, *1*, 458.

[33] R. D. Nikam, H. Hwang, *Adv. Funct. Mater.* **2022**, *32*, 2201749.

[34] X. Jing, F. Puglisi, D. Akinwande, M. Lanza, *2D Mater.* **2019**, *6*, 035021.

[35] E. W. Lim, R. Ismail, *Electronics* **2015**, *4*, 586.

[36] L. Jiang, Y. Shi, F. Hui, K. Tang, Q. Wu, C. Pan, X. Jing, H. Uppal, F. Palumbo, G. Lu, T. Wu, H. Wang, M. A. Villena, X. Xie, P. C. McIntyre, M. Lanza, *ACS Appl. Mater. Interfaces* **2017**, *9*, 39758.

[37] Y. Shen, W. Zheng, K. Zhu, Y. Xiao, C. Wen, Y. Liu, X. Jing, M. Lanza, *Adv. Mater.* **2021**, *n/a*, 2103656.

[38] R. V. Gorbachev, I. Riaz, R. R. Nair, R. Jalil, L. Britnell, B. D. Belle, E. W. Hill, K. S. Novoselov, K. Watanabe, T. Taniguchi, A. K. Geim, P. Blake, *Small* **2011**, *7*, 465.

[39] J. Wang, F. Ma, M. Sun, *RSC Adv.* **2017**, *7*, 16801.

[40] L. H. Li, E. J. G. Santos, T. Xing, E. Cappelluti, R. Roldán, Y. Chen, K. Watanabe, T. Taniguchi, *Nano Lett.* **2015**, *15*, 218.

[41] F.-C. Chiu, *Adv. Mater. Sci. Eng.* **2014**, *2014*, e578168.

[42] Y. Y. Illarionov, T. Knobloch, M. Jech, M. Lanza, D. Akinwande, M. I. Vexler, T. Mueller, M. C. Lemme, G. Fiori, F. Schwierz, T. Grasser, *Nat. Commun.* **2020**, *11*, 1.

[43] F.-C. Chiu, S. Mondal, T.-M. Pan, In *High-k Gate Dielectrics for CMOS Technology*, John Wiley & Sons, Ltd, **2012**, pp. 111–184.

[44] W. S. Lau, *ECS J. Solid State Sci. Technol.* **2012**, *1*, N139.

[45] S. M. Sze, K. K. Ng, *Physics of semiconductor devices*, Third edition., Wiley-Interscience, Hoboken, NJ, **2007**.

[46] A. Rose, *Phys. Rev.* **1955**, *97*, 1538.

[47] P. N. Murgatroyd, *J. Phys. Appl. Phys.* **1970**, *3*, 151.

[48] N. F. Mott, E. A. Davis, *Electronic Processes in Non-Crystalline Materials*, Oxford University Press, Oxford, New York, **2012**.

[49] F.-C. Chiu, C.-Y. Lee, T.-M. Pan, *J. Appl. Phys.* **2009**, *105*, 074103.

[50] B. L. Yang, P. T. Lai, H. Wong, *Microelectron. Reliab.* **2004**, *44*, 709.

[51] M. P. Hwang, Y. H. Wang, W. J. Chang, *J. Appl. Phys.* **1999**, *86*, 1488.

[52] S. Zaima, T. Furuta, Y. Koide, Y. Yasuda, M. Iida, *J. Electrochem. Soc.* **1990**, *137*, 2876.

[53] Y.-N. Xu, W. Y. Ching, *Phys. Rev. B* **1991**, *44*, 7787.

[54] H. Ibach, H. Lüth, *Solid-state physics: an introduction to principles of materials science*, 4th extensively updated and enlarged ed., Springer, Berlin ; New York, **2009**.

[55] S. O. Kasap, *Principles of electronic materials and devices*, 3rd ed., McGraw-Hill, Boston, **2006**.

[56] H.-W. Beckmann, W. Machon, W. Friedrich, Eds., *Elektrotechnik, Elektronik*, 585. Aufl., Bildungsverl. EINS, Troisdorf, **2015**.

[57] J. Zhang, R. Sun, D. Ruan, M. Zhang, Y. Li, K. Zhang, F. Cheng, Z. Wang, Z.-M. Wang, *J. Appl. Phys.* **2020**, *128*, 100902.

[58] F. Ducry, D. Waldhoer, T. Knobloch, M. Csontos, N. Jimenez Olalla, J. Leuthold, T. Grasser, M. Luisier, *Npj 2D Mater. Appl.* **2022**, *6*, 1.

[59] S. Menzel, U. Böttger, R. Waser, *J. Appl. Phys.* **2012**, *111*, 014501.

[60] S. A. Chekol, S. Menzel, R. W. Ahmad, R. Waser, S. Hoffmann-Eifert, *Adv. Funct. Mater.* **2022**, *32*, 2111242.

[61] Abraham. Savitzky, M. J. E. Golay, *Anal. Chem.* **1964**, *36*, 1627.

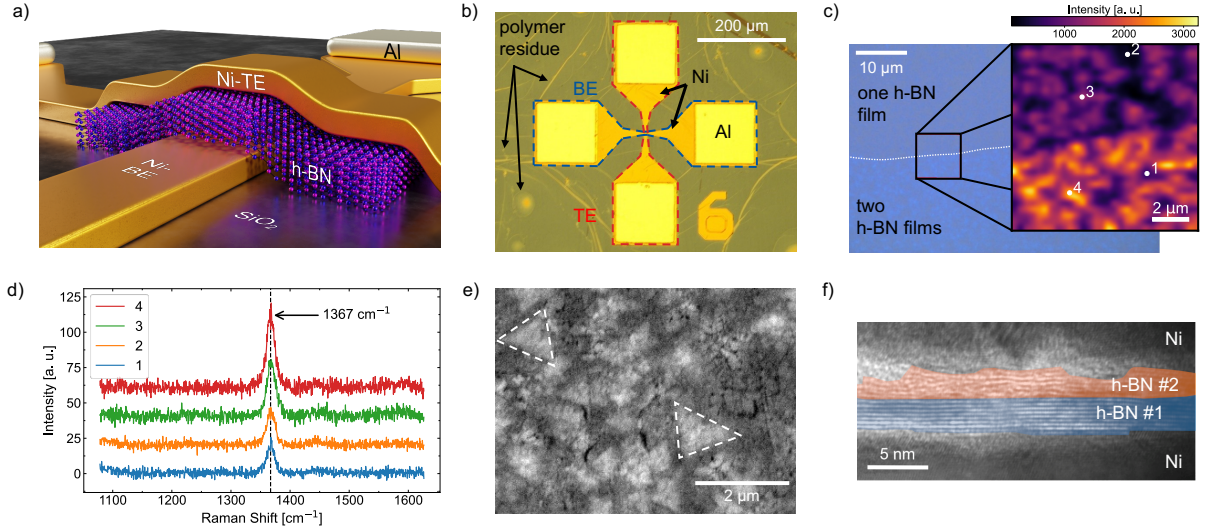


Figure 1: Device structure and material characterization. a) Schematic and b) optical microscope image of a Ni/h-BN/Ni cross-point device. c) Top-view optical microscope image of the as-transferred h-BN films showing the region where the first h-BN film and the stack of two h-BN films are visible. The boundary is marked by a white, dashed line. The inset shows a Raman map of the boundary region with integrated peak intensity of the characteristic h-BN E_{2g} peak. d) Four different Raman spectra, extracted from the respective positions marked in c). e) Top-view SEM image of the two stacked h-BN films after transfer on SiO_2/Si . The white, dashed triangles highlight probable nucleation sites of multilayer grains. f) HRTEM cross-section of a Ni/h-BN/Ni cross-point device. The first and second transferred h-BN film are marked in blue and orange, respectively.

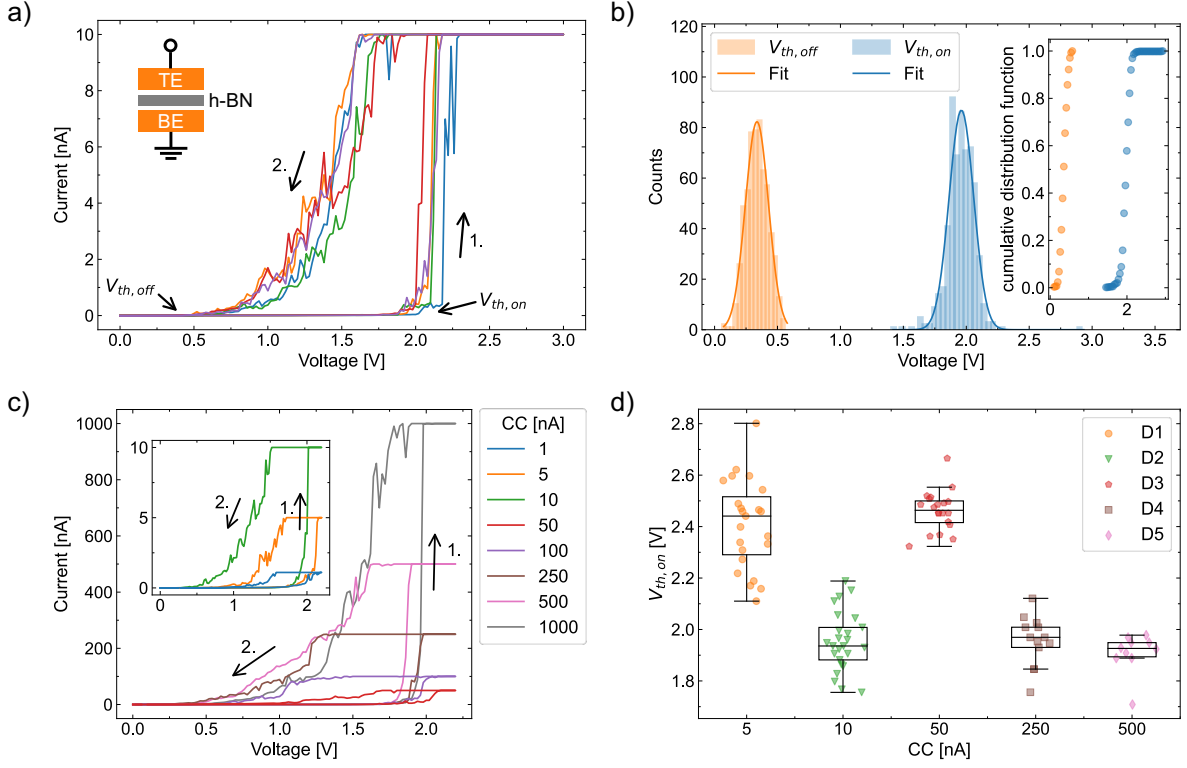


Figure 2: I - V characterization of Ni/h-BN/Ni memristors. a) Five subsequent I - V curves measured on a Ni/h-BN/Ni cross-point device showing TS. The arrows number one and two depict the voltage sweep direction, the others point on $V_{th,on}$ and $V_{th,off}$, respectively. The inset schematically shows the wiring during measurements. b) Histogram plot of $V_{th,on}$ and $V_{th,off}$ extracted from endurance measurement with ~ 600 subsequent I - V sweeps. The mean $V_{th,on}$ and $V_{th,off}$ of 2.0 ± 0.1 V and 0.3 ± 0.1 V, respectively, is extracted by fitting a Gaussian distribution to the histogram data. Inset: cumulative distribution function of $V_{th,off}$ and $V_{th,on}$. c) Eight subsequent I - V sweeps on the same device with different CCs showing TS. The CCs from 1 nA to 10 nA are plotted in the inset, the CCs from 50 nA to 1 μ A are shown in the main plot. The arrows indicate the voltage sweep directions. d) Statistical analysis of $V_{th,on}$ for different CCs and different devices (D1 – D5).

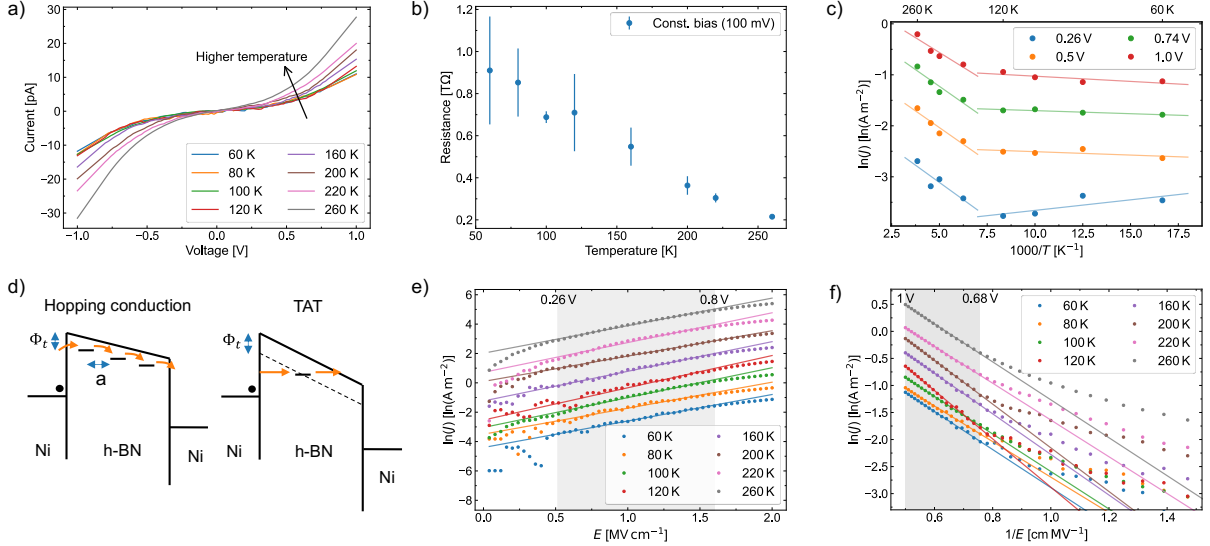


Figure 3: Conduction mechanism investigation of a Ni/h-BN/Ni device in HRS. a) Temperature-dependent, non-linear I - V curves (a Savitzky-Golay-filter was used to reduce noise, original data in Figure S7) in a temperature regime from 60 K to 260 K. b) Resistance vs. temperature measurement extracted by applying a constant voltage over time at different temperatures. c) Arrhenius plots extracted from the I - V data in a) showing two distinct linear regimes. The lines are linear fits to the data. d) Schematic band structure of a Ni/h-BN/Ni device for hopping conduction (left) and for TAT conduction (right). Φ_t is the trap depth in the hopping conduction and TAT equation, and a is known as the hopping distance in the hopping conduction equation. e) Hopping conduction plot with an artificial offset between the curves for better visibility. The data points with a gray background (0.26 V – 0.8 V) were found to fit best with a linear model. The lines are the corresponding linear fits. f) TAT conduction plot with an artificial offset between the curves. The most linear part of the data (gray background) is found to be between 0.68 V and 1 V. The lines are the corresponding linear fits.

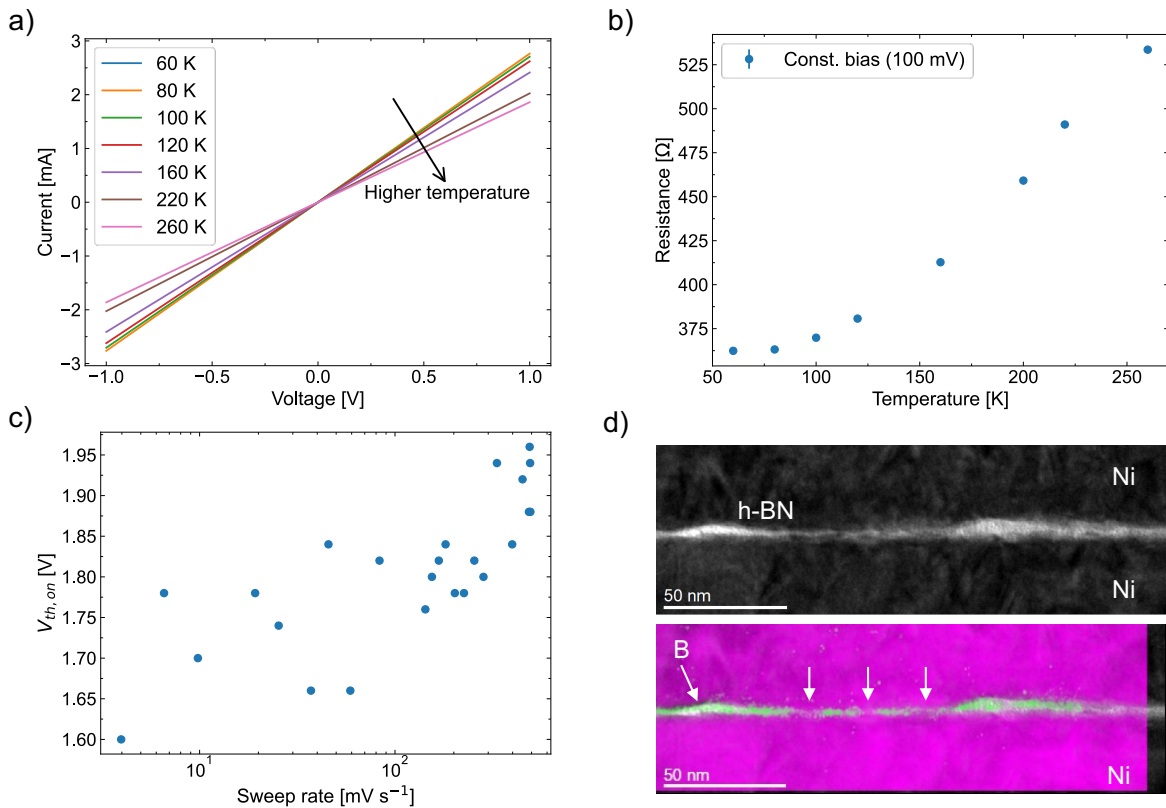


Figure 4: current conduction mechanism investigation of a device in a permanent LRS state after initial switching tests. a) Temperature-dependent I - V curves in a temperature regime from 60 K to 260 K. b) Resistance vs. temperature measurement. c) $V_{th,on}$ vs. sweep rate of a Ni/h-BN/Ni TS device in a HRS. $V_{th,on}$ decreases with decreasing sweep rate. d) TEM image of a memristor in a permanent LRS state. Top: cross section with h-BN sandwiched between two Ni electrodes. Bottom: overlay of EFTEM images of Ni (purple) and B (green). The Ni elemental map reveals direct contact of the Ni electrodes (indicated with white arrows). Gaps in the B layer are visible at the positions where the Ni electrodes are in direct contact.

Supporting Information

Hexagonal Boron Nitride Threshold Memristors with Symmetric Nickel Electrodes

Lukas Völkel¹, Dennis Braun¹, Melkamu Belete¹, Satender Kataria¹, Thorsten Wahlbrink², Ke Ran^{3,4},

Kevin Kistermann³, Joachim Mayer^{3,4}, Stephan Menzel⁵, Alwin Daus^{1*}, Max C. Lemme^{1,2*}

¹ Chair of Electronic Devices, RWTH Aachen University, Otto-Blumenthal-Str. 2, 52074 Aachen, Germany.

² AMO GmbH, Advanced Microelectronic Center Aachen, Otto-Blumenthal-Str. 25, 52074 Aachen, Germany.

³ Central Facility for Electron Microscopy (GFE), RWTH Aachen University, Ahornstr. 55, 52074, Aachen, Germany.

⁴ Ernst Ruska-Centre for Microscopy and Spectroscopy with Electrons (ER-C 2), Forschungszentrum Jülich, 52425, Jülich, Germany.

⁵ Peter Gruenberg Institute (PGI-7), Forschungszentrum Juelich GmbH and JARA-FIT, 52425 Juelich, Germany.

Section S1: Schematic process flow

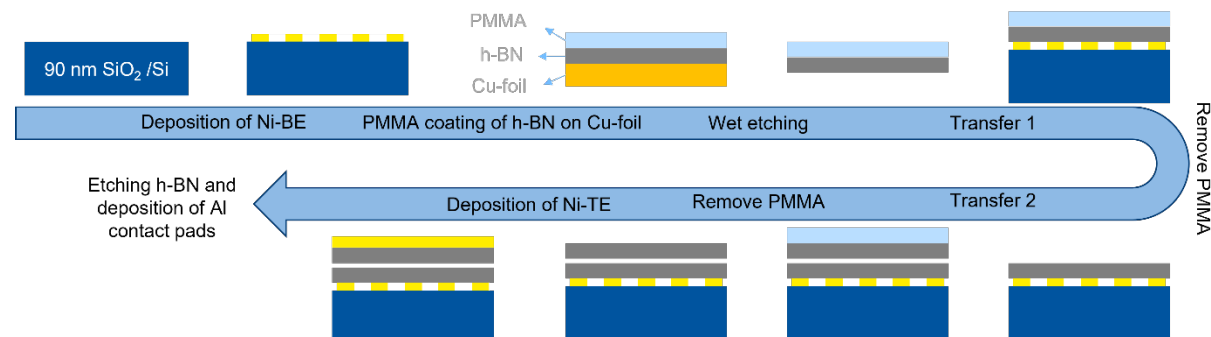


Figure S1: Schematic process flow. BE: Bottom electrode, TE: top electrode, Cu: copper, Al: aluminum, Ni: nickel.

Section S2: Current-voltage measurements on devices without h-BN

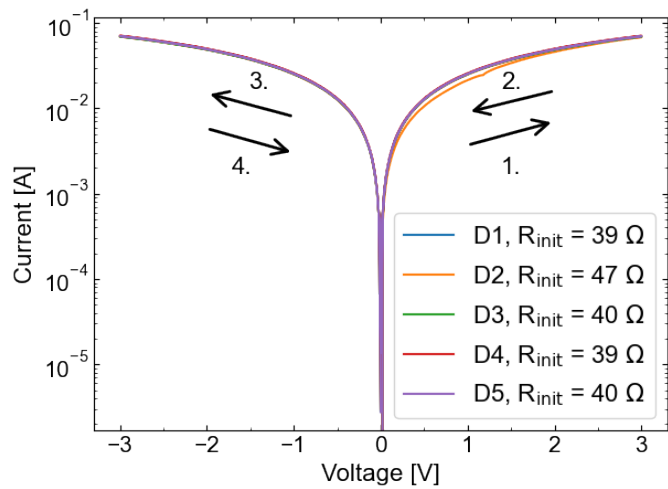


Figure S2: *I*-*V* curves measured of five different Ni/Ni memristors D1-D5.

To measure the possible influence of a nickel oxide layer between the Ni electrodes or between Ni and the Al contact pads on the RS behavior, we measure the initial resistance of devices without h-BN between the electrodes and subsequently apply a positive and a negative sweep with a maximum voltage of ± 3 V. The initial resistance of all devices is only a few Ω and none of the devices show resistive switching. Thus, we can exclude an influence of the electrode material system on our resistive switching measurements.

Section S3: Histogram of h-BN E_{2g} peak position from Raman map spectra

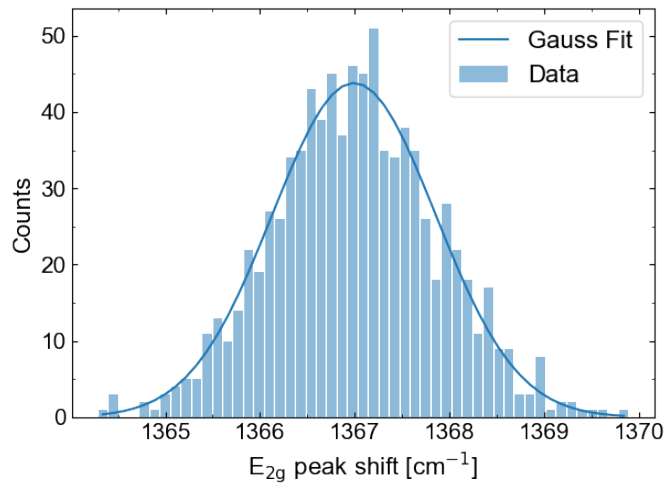


Figure S3: Histogram of extracted E_{2g} -peak position of all spectra in the Raman map. The peak positions are extracted by fitting a Lorentz-Peak to each Raman spectrum. A Gaussian distribution function with the center at 1367.0 cm^{-1} and a distribution width of $\sigma = 0.9\text{ cm}^{-1}$ is fitted to the histogram data, which corresponds to 3-layer to bulk h-BN^[1].

Section S4: HRTEM and van der Waals spacing

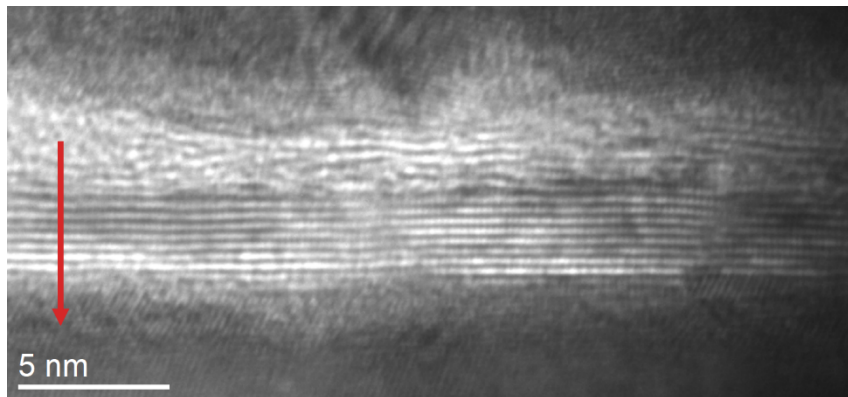


Figure S4-1: HRTEM image with the arrow indicating the position for line profile extraction.

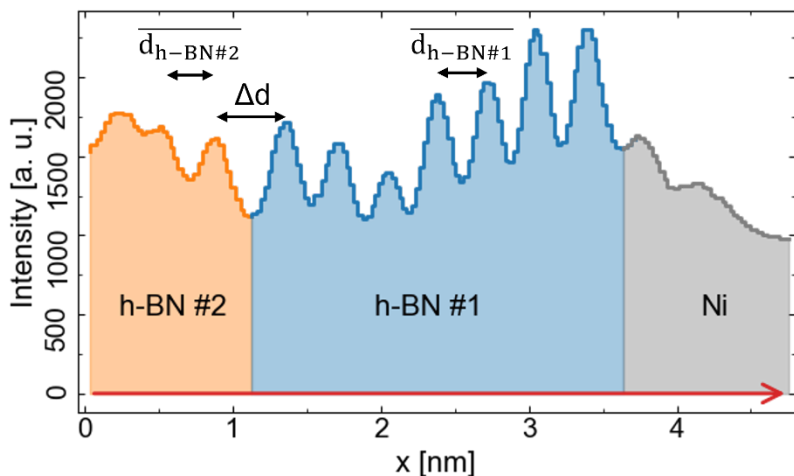


Figure S4-2: From HRTEM extracted line-profile. The orange, blue and gray regions are identified as h-BN film #2, h-BN film #1, and the Ni bottom electrode, respectively. $\overline{d}_{h\text{-BN}\#1} = 0.321 \pm 0.029$ nm is the mean interlayer distance of two adjacent h-BN layers in h-BN film 1, $\overline{d}_{h\text{-BN}\#2} = 0.340 \pm 0.016$ nm is the mean interlayer distance of two adjacent h-BN layers in film 2, and $\Delta d = 0.479$ nm is the spacing between h-BN film 1 and 2. The measured interlayer distance agrees with other literature values^[2,3], whereas Δd is almost 30 % bigger.

Section S5: *I*-*V* Curves of endurance measurement

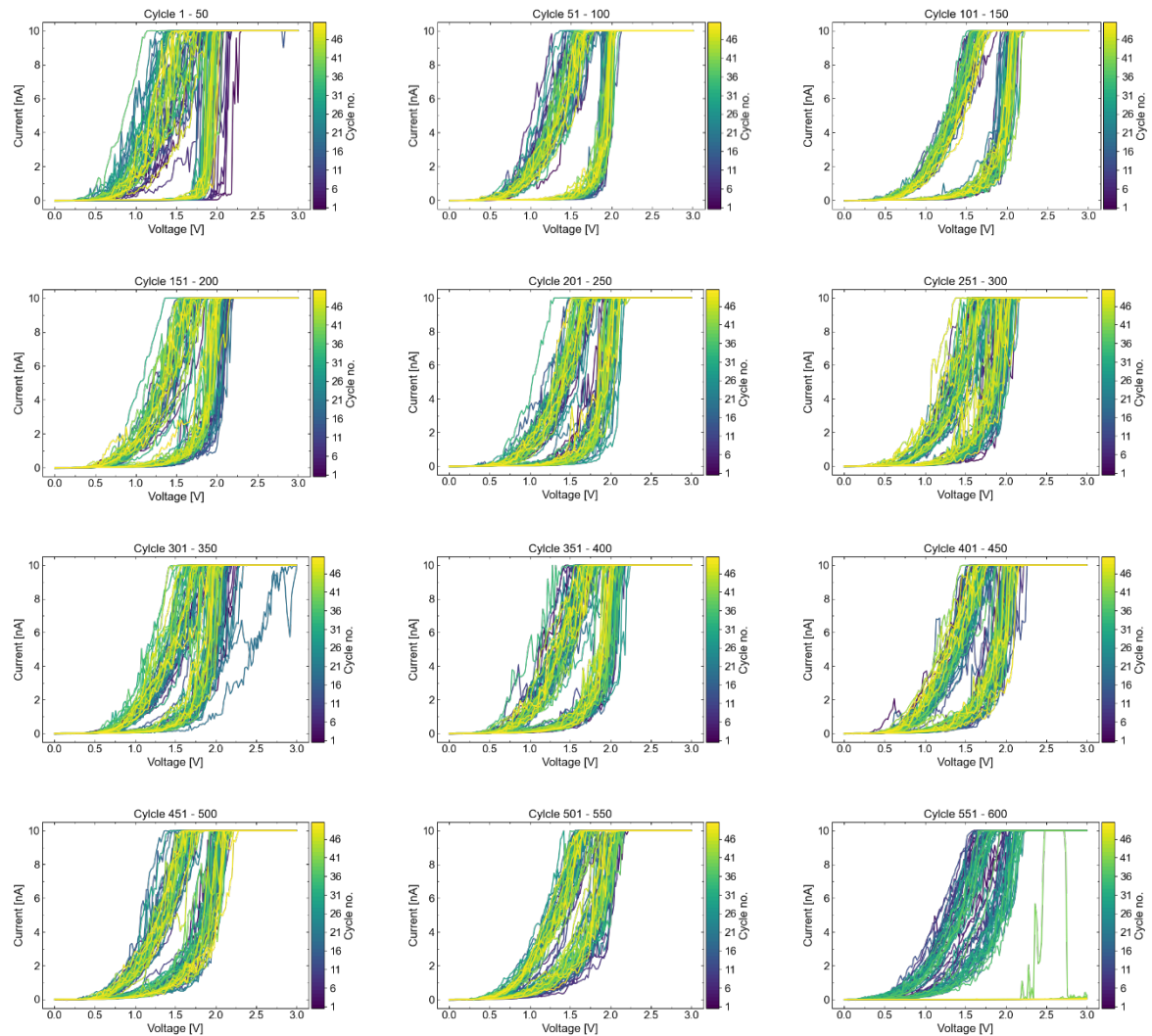


Figure S5: Complete set of *I*-*V* cycles measured during the endurance measurement. Every plot contains 50 cycles. The title of the plots denotes the respective cycle number range.

Section S6: Comparison of device performance with other literature

$I_{cc,max}/I_{cc,min}$ [A]	max. On/Off ratio	max. DC Endurance	Electrode material (BE/TE)	h-BN thickness	CMOS- compatible configuration	Reference
10^2	$5 \cdot 10^4$	5	Cu/Pt	3.5 nm	No (C-AFM)	[4]
10	$5 \cdot 10^5$	7	Pt/Ag	1.5 nm	No	[5]
5	$5 \cdot 10^7$	-	Ag/Pt, Ag/Ag	0.33 nm	No, No	[6]
10^2	10^4	2	Ti/Cu	5-7/15-20 layers	Yes	[7]
0	10^5	4	Fe/Ag	~ 15 layers	No	[8]
0	10^3	-	Fe/Ag	> 10 layers	No	[9]
0	$5 \cdot 10^6$	\sim few 10	Ag/Au	9-15 layers	No	[10]
10^9	10^{11}	-	Ag/Ag	1.5 nm	No	[11]
0	$5 \cdot 10^5$	\sim several 10	Ag/Pt, Pt/Pt	1.5 nm	No, Yes	[11]
10^2	$5 \cdot 10^4$	~ 300	Ti/Cu	1.8 nm	Yes	[12]
0	10^5	\sim few 10	Ag/Au	15-18 layers	No	[13]
0	10^4	-	Au/Ni, Ni/Ni, Pt/Ni	1 layer	No (common BE)	[14]
10^5	10^8	100	Pt/Ag, Pt/Gr/Ag	1 layer	No	[15]
10^3	$5 \cdot 10^5$	588	Ni/Ni	5 ± 1 nm	Yes	This work

Table S6: Benchmarking table of publications showing TRS in h-BN-based resistive switching devices.

$I_{cc,max}/I_{cc,min}$ denote the current compliance window in which the device shows threshold resistive switching behavior. A CMOS-compatible configuration includes a CMOS compatible material stack as well as an application-near device structure like cross point devices. Devices with a common bottom electrode or conductive atomic force microscopy (C-AFM) investigations are considered as not CMOS compatible configurations.

Section S7: Temperature dependent *I*-*V* curves of Device in HRS

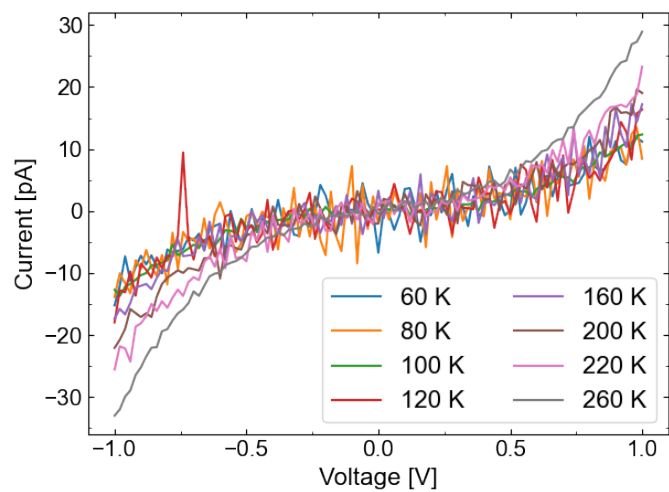


Figure S7: Unfiltered *I*-*V* data of the temperature dependent measurements of a Ni/h-BN/Ni device in HRS. The *I*-*V* curves shown in the main paper are smoothed with a Savitzky-Golay filter^[16].

Section S8: Algorithm to get the most linear region of a curve according to R²-criterion

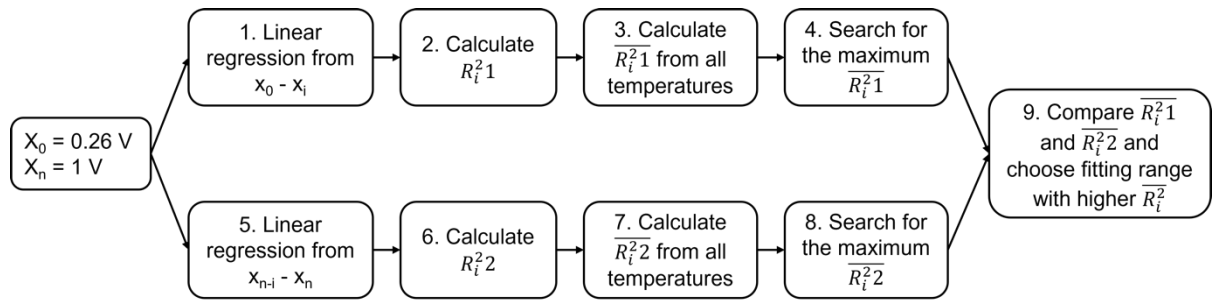


Figure S8: Flow-chart of algorithm to get the most linear region in our *I*-*V* curve.

The R²-value is defined as the ratio of the squared deviation of the fitted values from the measured values and the squared deviation of the measured values from the global mean of a linear regression model, and normalized to an absolute value between 0 and 1^[17,18]. A value close to 1 denotes a good match of the linear fit to the data, whereas a value close to 0 denotes a bad match of the linear fit to the data.

We exclude the voltage range between 0 V and 0.26 V from our fits because in Figure 3c in the main paper one can see that at a voltage of 0.26 V the measurement noise is high, which will lead to inconsistent results. This means for the fitting algorithm that the minimum fitting range is fixed to $x_0 = 0.26$ V or its corresponding x-value of the linearized *I*-*V* data corresponding to the conduction mechanism formula. The following steps are performed to find the most linear region in our curves according to the R²-criterion with the constraint that either the maximum or the minimum of the fitting range is fixed:

1. Perform a linear regression from x_0 to x_i for each temperature, where x_i is the i -th data point and its range is $i = \{10, 11, 12, \dots, n - 1, n\}$, where n is the total number of data points.
2. Calculate $R_i^2 1$ for each linear regression. With $i \geq 10$ the smallest linear regression includes 10 data points.
3. Calculate $\overline{R_i^2 1}$, the mean $R_i^2 1$ from all temperatures.
4. Search for the maximum $\overline{R_i^2 1}$.
5. Perform a linear regression from x_{n-i} to x_n , with $i = \{10, 11, 12, \dots, n - 1, n\}$.
6. Calculate $R_i^2 2$ for each linear regression.
7. Calculate $\overline{R_i^2 2}$, the mean $R_i^2 2$ from all temperatures.
8. Search for the maximum $\overline{R_i^2 2}$.
9. Compare $\overline{R_i^2 1}$ and $\overline{R_i^2 2}$ and choose the fitting range with the higher $\overline{R_i^2}$.

The fitting range with the highest $\overline{R_l^2}$ corresponds, according to the R^2 -criterion, to the most linear region in the curves. The algorithm is summarized in Figure S8.

Section S9: Discussion of various current conduction mechanisms

In this section we discuss the applicability of the Poole Frenkel model, the space charge limited conduction (SCLC) model, the nearest neighbor hopping (NNH) and the Mott variable range hopping (VRH) model to our temperature dependent I - V data in the HRS.

The Poole Frenkel CCM assumes that electrons are thermally emitted from traps into the conduction band of the dielectric material and it has a characteristic electric field and temperature dependence of^[19]

$$J \sim E \cdot \left[\frac{-q(\Phi_T - \sqrt{\frac{qE}{\pi\epsilon_r\epsilon_0}})}{k_B T} \right], \quad (s1)$$

where E is the electric field, q is the elementary charge, Φ_T is the trap depth, ϵ_r is the dielectric constant, ϵ_0 is the vacuum permittivity, and k_B is the Boltzmann constant. Considering equation (s1), a plot of $\ln(J/E)$ vs. \sqrt{E} should be linear. The electric field is calculated by dividing the applied voltage by the h-BN film thickness extracted from the HRTEM image in Figure 1f in the main paper. The Poole-Frenkel plot is shown in Figure S9-1. We found the most linear region in the Poole-Frenkel plot between 0.56 V and 1 V. According to equation (s1), we can calculate the dielectric constant of our h-BN film with the slope extracted by the linear regression. The calculated dielectric constants for all temperatures can be found in Table S9-1. We see that the dielectric constant highly depends on the temperature and additionally has values more than 60 times higher than the literature value of $\epsilon_r = 5$ ^[20]. Thus, we exclude the Poole Frenkel CCM as the responsible CCM in our devices.

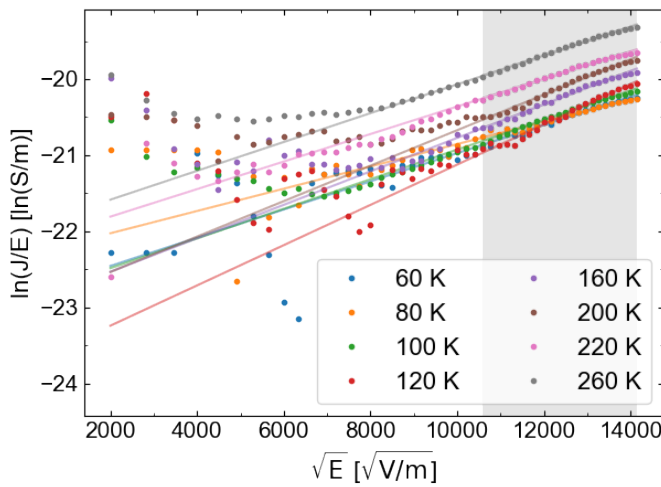


Figure S9-1: Poole-Frenkel plot for all temperatures. The data points with a gray background ($10600 \sqrt{V/m}$ - $14142 \sqrt{V/m}$, which corresponds to $0.56 \text{ V} - 1 \text{ V}$) fit best to a linear model. The lines are the corresponding linear fits.

Temperature [K]	Dielectric constant ϵ_r
-----------------	----------------------------------

60	6281
80	5644
100	2047
120	769
160	626
200	357
220	489
260	319

Table S9-1: Extracted dielectric constants for all temperatures.

The SCLC theory predicts the current density between two plane, parallel electrodes to be split in three regimes, the ohmic conduction current ($J_{Ohm} \sim V$), the trap-filled limit current ($J_{TFL} \sim V^2$) and Child's law ($J_{Child} \sim V^2$), where the current densities depend on the applied voltage as follows:^[21]

$$J_{Ohm} = qn_0\mu \frac{V}{d}, \quad (s2)$$

$$J_{TFL} = \frac{9}{8}\mu\epsilon_r\epsilon_0\theta_0 \frac{V^2}{d^3}, \quad (s3)$$

$$J_{Child} = \frac{9}{8}\mu\epsilon_r\epsilon_0 \frac{V^2}{d^3}. \quad (s4)$$

n_0 is the concentration of the free charge carriers in thermal equilibrium, μ is the charge carrier mobility, θ_0 is the ratio of the effective density of states in the conduction band and the density of traps inside the h-BN, d is the distance between the electrodes, and V is the applied voltage. Between J_{TFL} and J_{Child} is a transition region where $J \sim V^x$ with $x > 2$. We expect to be only in the first two regions, as we apply relatively low voltages. For this CCM we do not apply our algorithm for maximized R^2 -value but adapt it to find the fitting range leading to a slope of 2 (with a fixed maximum of the fitting range at 1 V) and the fitting range leading to a slope of 1 (with a fixed minimum of the fitting range at the second data point at 0.06 V). This procedure leads to an overlap of the fitting ranges, so we adjust the overlap region manually in a way that there is no overlap and at the same time the R^2 values remain close to 1. In Table 9-2 the extracted slopes of the linear regression fits can be found. With the equations (s2) and (s3) one can extract the mobility of the charge carriers from the intercept of the fitted lines. However, in the case of the ohmic conduction region, we must estimate n_0 to calculate the mobility, and in the case of the TFL region, we must estimate θ . We will only extract the mean mobility from all temperatures as we must estimate the values for θ and n_0 anyways, which is a relatively big error source. A. Rose^[22] gives an approximate value for θ of $\sim 10^{-7}$. With this, we estimate the mean mobility in the TFL region of all temperatures to be $\mu_{mean} = (1.2 \pm 0.45) \cdot 10^{-4} \frac{cm^2}{Vs}$, which is comparable to the values extracted by Chiu et. al.^[23,24] for other insulators. However, the extraction of a realistic value for the mobility in the ohmic region is not possible. We found no applicable literature value for n_0 . To get a first estimation of the mobility we set n_0 to 1. This results in a mean mobility of $\mu_{mean} \approx 5 \cdot 10^{13} \frac{cm^2}{Vs}$. This means, n_0 must be in the order of $10^{17} \frac{1}{cm^3}$.

to get a comparable value for the mobility in both regions, which is unrealistic for a wide-bandgap, insulating material like h-BN at low temperatures (< 260 K).

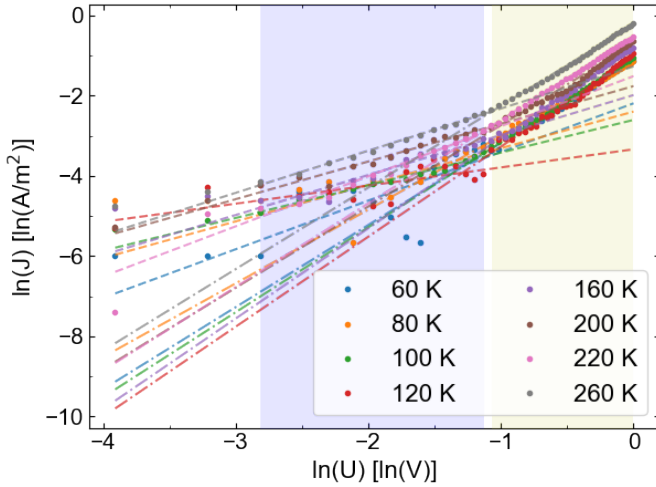


Figure S9-2: Characteristic space charge limited CCM plot for all temperatures. The blue and yellow regions mark the fitting range for ohmic conduction regime and trap-filled limit current regime, respectively. The dashed and dash-dotted lines are the fits of the blue and yellow region, respectively.

T [K]	Slope blue region	R ² blue region	Slope yellow region	R ² yellow region
60	1.21	0.448	2.05	0.993
80	0.91	0.526	1.84	0.994
100	0.81	0.975	2.12	0.999
120	0.45	0.368	2.24	0.985
160	1.00	0.916	2.25	0.996
200	0.94	0.940	2.03	0.987
220	1.24	0.979	2.08	0.999
260	1.05	0.995	2.03	0.998

Table 9-2: Extracted slopes of linear regression fits for different temperatures in respective regions of the characteristic SCLC plot.

The NNH and Mott VRH mechanisms assume electrons hopping through the dielectric from traps to traps via nearest neighboring traps with a certain barrier height, or traps with a variable (wider) distance but possibly a lower energy barrier, respectively. The models describe a characteristic temperature dependence of^[25]

$$\sigma = \sigma_0 \cdot e^{-(T_0/T)^\beta}, \quad (s5)$$

where σ is the conductance, σ_0 is the conductivity at a certain temperature T_0 , T is the temperature, and β is a parameter dependent on the model under consideration. In the NNH and Mott VRH models $\beta = 1$ and $\beta = \frac{1}{4}$, respectively. In contrast to the CCMs discussed before we need to measure the temperature dependent conductance of our devices to apply these models. This is done by calculating the inverse of the resistance shown in Figure 3b in the main paper, which was measured at a voltage of 0.1 V. By extracting T_0 one can calculate the hopping energy^[26]

$$E_h(T) = \frac{1}{4}k_b T^{3/4} T_0^{1/4}, \quad (s6)$$

which reflects the energy barrier between defects. From equation (s5), one expects a linear behavior when the natural logarithm of the conductance is plotted over $\frac{1}{T^\beta}$. The characteristic plots for NNH and Mott VRH are shown in Figures S8-3 and S8-4, respectively. Both plots exhibit a nonlinear behavior over the full temperature range, but a linear region for temperatures ≥ 160 K can be identified in both plots. In the smaller temperature range the data points seem to be linear, too. However, having a closer look to the fit statistics let us exclude these temperatures from our further analysis due to the high noise in the measurement (compare argumentation to the Arrhenius plot discussed in the main paper). According to equation (s5), T_0 depends on the slope of the linear fit and σ_0 is related to the intercept of the linear fit. Conducting a linear fit for temperatures ≥ 160 K in the NNH plot we get $T_0 = -48$ K and $\sigma_0 = 23$ pS. The negative T_0 would lead to a negative hopping energy, which is physically not meaningful. Thus, we exclude NNH as a possible conduction mechanism.

We find $T_0 = 8.55 \cdot 10^5$ K and $\sigma_0 = 9$ nS by fitting the region for $T \geq 120$ K in the Mott VRH characteristic plot. According to equation (s6), we get a mean $E_h = 36 \pm 6$ meV.

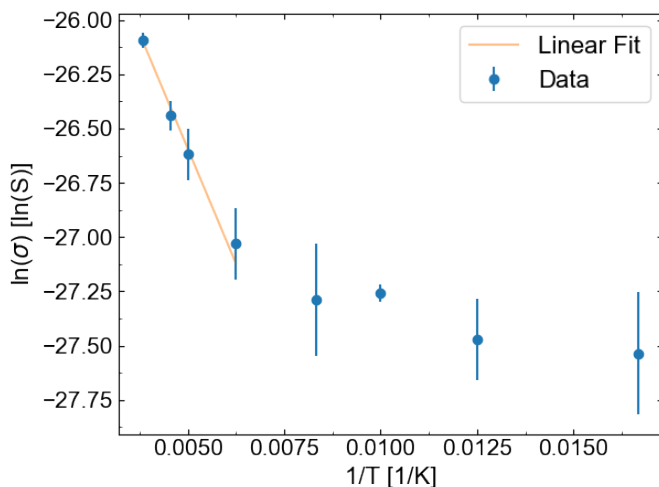


Figure S9-3: Nearest neighbor hopping plot.

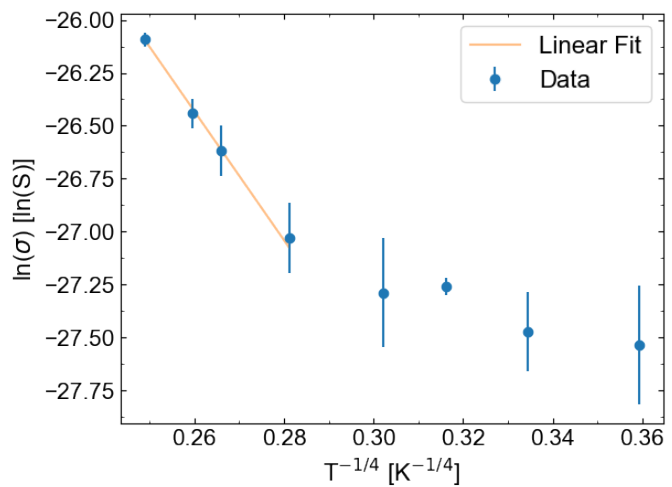


Figure S9-4: Mott variable range hopping plot.

Section S10: Hopping conduction

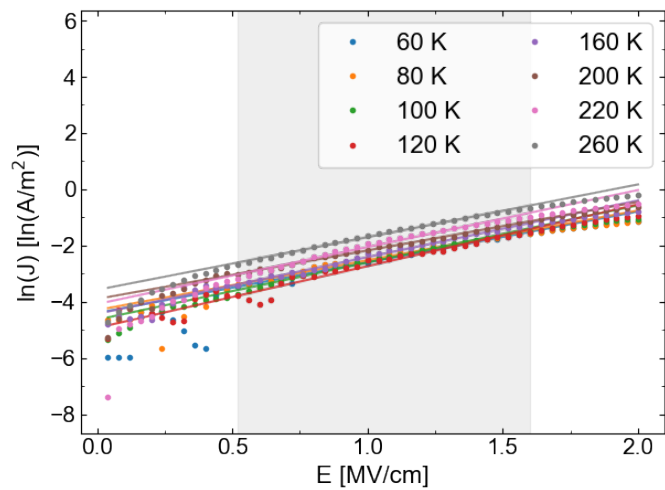


Figure S10: Characteristic hopping conduction plot without an additional offset.

Section S11: Trap assisted tunneling

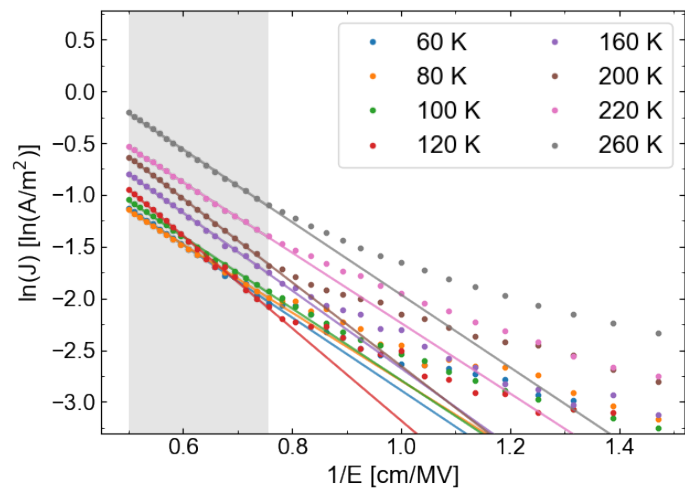


Figure S11: Characteristic trap assisted tunneling plot without an additional offset.

Section S12: Temperature dependent I-V measurements of a device in permanent LRS

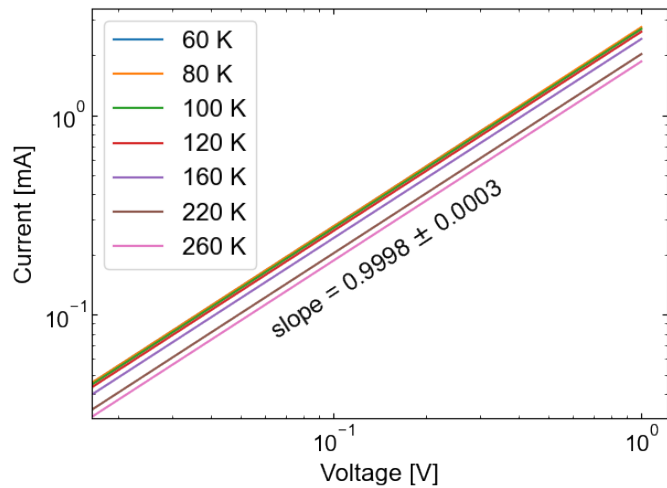


Figure S12: Double-logarithmic plot of I-V curves shown in Figure 4a in the main paper. All curves show clear linear behavior with a mean slope of 0.9998 ± 0.0003 A/V.

Section S13: Energy filtered TEM (EFTEM) images

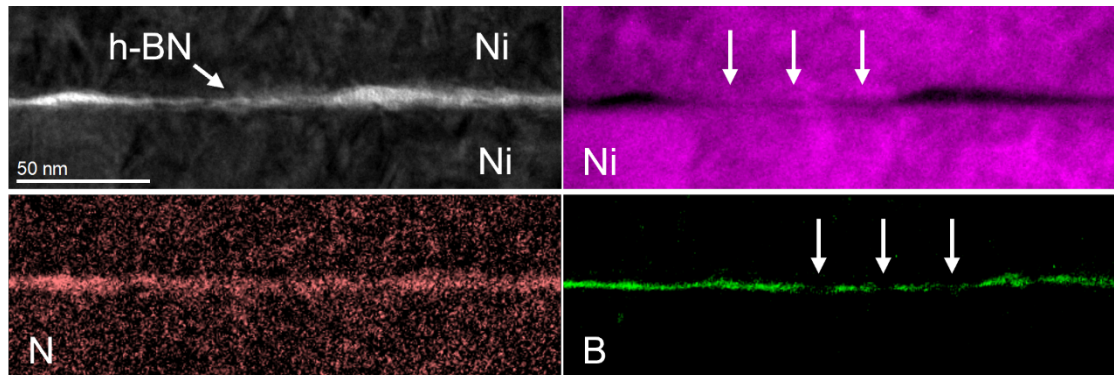


Figure S13: Cross-section TEM and EFTEM images of nickel, nitrogen, and boron.

Due to drift of the TEM-lamella between the different EFTEM measurements the marked features do not appear at the same positions. However, referencing the EFTEM maps to the cross-section TEM image let us create the overlay-image shown in Figure 4d in the main paper. The nitrogen map reveals no distinct defects in the h-BN film.

References:

- [1] L. H. Li, J. Cervenka, K. Watanabe, T. Taniguchi, Y. Chen, *ACS Nano* **2014**, *8*, 1457.
- [2] J. Wang, F. Ma, M. Sun, *RSC Adv.* **2017**, *7*, 16801.
- [3] L. H. Li, E. J. G. Santos, T. Xing, E. Cappelluti, R. Roldán, Y. Chen, K. Watanabe, T. Taniguchi, *Nano Lett.* **2015**, *15*, 218.
- [4] A. Ranjan, N. Raghavan, S. J. O'Shea, S. Mei, M. Bosman, K. Shubhakar, K. L. Pey, *Sci. Rep.* **2018**, *8*, 1.
- [5] G. Dastgeer, H. Abbas, D. Y. Kim, J. Eom, C. Choi, *Phys. Status Solidi RRL – Rapid Res. Lett.* **2020**, *15*, 2000473.
- [6] R. D. Nikam, K. G. Rajput, H. Hwang, *Small* **2021**, *17*, 2006760.
- [7] C. Pan, Y. Ji, N. Xiao, F. Hui, K. Tang, Y. Guo, X. Xie, F. M. Puglisi, L. Larcher, E. Miranda, L. Jiang, Y. Shi, I. Valov, P. C. McIntyre, R. Waser, M. Lanza, *Adv. Funct. Mater.* **2017**, *27*, 1604811.
- [8] F. Hui, M. A. Villena, W. Fang, A.-Y. Lu, J. Kong, Y. Shi, X. Jing, K. Zhu, M. Lanza, *2D Mater.* **2018**, *5*, 031011.
- [9] M. A. Villena, F. Hui, X. Liang, Y. Shi, B. Yuan, X. Jing, K. Zhu, S. Chen, M. Lanza, *Microelectron. Reliab.* **2019**, *102*, 113410.
- [10] B. Yuan, X. Liang, L. Zhong, Y. Shi, F. Palumbo, S. Chen, F. Hui, X. Jing, M. A. Villena, L. Jiang, M. Lanza, *Adv. Electron. Mater.* **2020**, *6*, 1900115.
- [11] S. Chen, M. R. Mahmoodi, Y. Shi, C. Mahata, B. Yuan, X. Liang, C. Wen, F. Hui, D. Akinwande, D. B. Strukov, M. Lanza, *Nat. Electron.* **2020**, *3*, 638.
- [12] Y. Shi, C. Pan, V. Chen, N. Raghavan, K. L. Pey, F. M. Puglisi, E. Pop, H.-P. Wong, M. Lanza, In *2017 IEEE International Electron Devices Meeting (IEDM)*, **2017**, p. 5.4.1-5.4.4.
- [13] Y. Shi, X. Liang, B. Yuan, V. Chen, H. Li, F. Hui, Z. Yu, F. Yuan, E. Pop, H.-S. P. Wong, M. Lanza, *Nat. Electron.* **2018**, *1*, 458.
- [14] Y. Li, Z. Cui, Y. He, H. Tian, T. Yang, C. Shou, J. Liu, *Appl. Phys. Lett.* **2022**, *120*, 173104.
- [15] R. D. Nikam, H. Hwang, *Adv. Funct. Mater.* **2022**, *32*, 2201749.
- [16] Abraham. Savitzky, M. J. E. Golay, *Anal. Chem.* **1964**, *36*, 1627.
- [17] N. R. Draper, H. Smith, *Applied regression analysis*, 3rd ed., Wiley, New York, **1998**.
- [18] J. L. Devore, *Probability and statistics for engineering and the sciences*, Eighth edition., Brooks/Cole, Cengage Learning, Boston, MA, **2012**.
- [19] E. W. Lim, R. Ismail, *Electronics* **2015**, *4*, 586.
- [20] Y. Y. Illarionov, T. Knobloch, M. Jech, M. Lanza, D. Akinwande, M. I. Vexler, T. Mueller, M. C. Lemme, G. Fiori, F. Schwierz, T. Grasser, *Nat. Commun.* **2020**, *11*, 1.
- [21] F.-C. Chiu, S. Mondal, T.-M. Pan, In *High-k Gate Dielectrics for CMOS Technology*, John Wiley & Sons, Ltd, **2012**, pp. 111–184.
- [22] A. Rose, *Phys. Rev.* **1955**, *97*, 1538.
- [23] F.-C. Chiu, C.-Y. Lee, T.-M. Pan, *J. Appl. Phys.* **2009**, *105*, 074103.
- [24] F.-C. Chiu, *J. Appl. Phys.* **2007**, *102*, 044116.
- [25] N. F. Mott, E. A. Davis, *Electronic Processes in Non-Crystalline Materials*, Oxford University Press, Oxford, New York, **2012**.
- [26] S. Ravi, M. Kar, *Phys. B Condens. Matter* **2004**, *348*, 169.